PNAS RESEARCH ARTICLE | BIOPHYSICS AND COMPUTATIONAL BIOLOGY

Quantifying a light-induced energetic change in bacteriorhodopsin by force spectroscopy

David R. Jacobson[a,1] and Thomas T. Perkins[a,b,2]

Edited by William DeGrado, University of California San Francisco, San Francisco, CA; received August 10, 2023; accepted December 26, 2023

Ligand-induced conformational changes are critical to the function of many membrane proteins and arise from numerous intramolecular interactions. In the photocycle of the model membrane protein bacteriorhodopsin (bR), absorption of a photon by retinal triggers a conformational cascade that results in pumping a proton across the cell membrane. While decades of spectroscopy and structural studies have probed this photocycle in intricate detail, changes in intramolecular energetics that underlie protein motions have remained elusive to experimental quantification. Here, we measured these energetics on the millisecond time scale using atomic-force-microscopy-based single-molecule force spectroscopy. Precisely, timed light pulses triggered the bR photocycle while we measured the equilibrium unfolding and refolding of the terminal 8-amino-acid region of bR's G-helix. These dynamics changed when the EF-helix pair moved ~9 Å away from this end of the G helix during the "open" portion of bR's photocycle. In ~60% of the data, we observed abrupt light-induced destabilization of 3.4 ± 0.3 kcal/mol, lasting 38 ± 3 ms. The kinetics and pH-dependence of this destabilization were consistent with prior measurements of bR's open phase. The frequency of light-induced destabilization increased with the duration of illumination and was dramatically reduced in the triple mutant (D96G/F171C/F219L) thought to trap bR in its open phase. In the other ~40% of the data, photoexcitation unexpectedly stabilized a longer-lived putative misfolded state. Through this work, we establish a general single-molecule force spectroscopy approach for measuring ligand-induced energetics and lifetimes in membrane proteins.

membrane proteins | atomic force microscopy | photochemistry | single-molecule force spectroscopy | protein folding

Significance

Membrane-protein dynamics underlie numerous critical biological functions, including signaling and transport. Precise quantification of the energetics that drive these conformational transitions is a long-sought goal needed to complement extensive atomic-scale structural information. Recent advances have shown membrane-protein folding energetics and the energetic consequences of point mutations can be quantified via mechanical unfolding using atomic force microscopy. This single-molecule method is enabled by custom-modified ultrashort cantilevers with 1-μs resolution and site-specific attachment. Here, we extend this technique by triggering bacteriorhodopsin's photocyle using sub-ms light pulses to quantify the destabilization of a critical helix-helix interaction modulated during bacteriorhodopsin's "open" phase, prior to reprotonation. The open phase's kinetics, its pH dependency, and the effect of a well-studied triple-mutant were also measured.

Conformational changes due to ligand–protein interactions are central to the function of many membrane proteins, including the pharmaceutically important G-protein-coupled receptors (1–3). An excellent model system for studying such ligand-induced conformational changes is the photocycle of bacteriorhodopsin (bR) from *Halobacterium salinarum* (4). Extensive spectroscopic and structural studies have revealed that bR's retinal ligand isomerizes upon light absorption, leading the protein to execute an intricate cycle of conformational changes that result in pumping a proton across the cell membrane (Fig. 1*A*). Notwithstanding atomically resolved structures of these photocycle phases (5–7), precise quantification of the energetic interactions that drive these conformation changes remain elusive (3). Yet, such quantification is critical for a more complete biophysical understanding of how ligand–protein interactions trigger complex changes in membrane protein structure and how these dynamics are disrupted by mutations.

At the center of bR's photocycle is the retinal ligand nestled within bR's seven transmembrane helices and covalently bound to Lys^{216} of the G helix via a Schiff base. Upon light absorption, the retinal isomerizes from the all-*trans* to 13-*cis*,15-*anti* configuration, which in turn leads to a concerted series of conformational changes in the surrounding protein. These changes modify the chemical environment of key amino acids, resulting in a proton being released from the Schiff base to the extracellular environment. Next, the Schiff base is reprotonated by opening up a channel from the retinal to the cytoplasm via a ~9-Å rotation of the F and E helices away from the G helix (7) (Fig. 1*B*), a phase referred to as "open" in the literature (8) and dominated by the spectroscopic "N" state (9).

The detailed conformational and kinetic course of the photocycle has been a subject of intense interest since Racker and Stoeckenius first reported bR's proton-pumping activity in 1974 (10). Methods employed have included spectroscopy (11–14), biochemical analysis (15, 16), electron and neutron diffraction (17–19), electron paramagnetic resonance (20–22), and x-ray crystallography (23–26). Recently, time-resolved crystallography experiments have allowed for direct visualization of each step of the photocycle (5–7, 27). In parallel, high-speed atomic-force microscopy (AFM) has imaged the motion of bR's interhelical loops under non-crystalline, biologically relevant conditions, confirming key conclusions about structure and kinetics (9, 28–30). Importantly, both structural and AFM

Author contributions: D.R.J. and T.T.P. designed research; D.R.J. performed research; D.R.J. analyzed data; and D.R.J. and T.T.P. wrote the paper.

The authors declare no competing interest.

This article is a PNAS Direct Submission.

[1]Present address: Department of Chemistry, Clemson University, Clemson, SC 29634.

[2]To whom correspondence may be addressed. Email: tperkins@colorado.edu.

This article contains supporting information online at https://www.pnas.org/lookup/suppl/doi:10.1073/pnas.2313818121/-/DCSupplemental.

Published February 7, 2024.

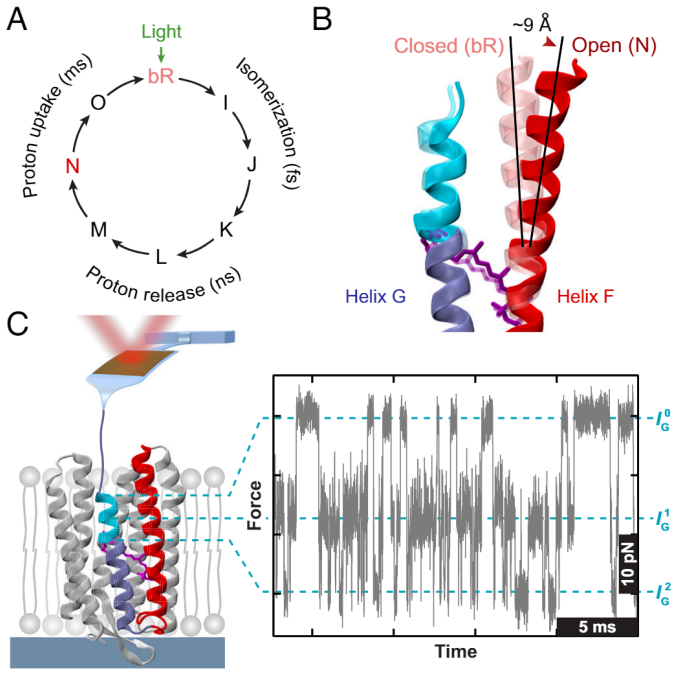

Fig. 1. The photocycle of bR probed by single-molecule force spectroscopy. (*A*) A diagram illustrating the series of spectroscopically resolvable states (I through O) that exist on increasingly long timescales upon light absorption by bR. The final states occur on the ms timescale accessible to advanced AFM methods. (*B*) Structural rendering derived from time-resolved x-ray crystal structures of Weinert et al. (7) shows the rotation of the F helix when bR transitions from its closed phase (transparent) to the ms-timescale, open N phase (solid), leading to a significant gap between helix F (red) and the 8-amino-acid portion of helix G (cyan) probed in this study [PDB 6RQP (closed) and 6RPH (open)]. (*C*) Illustration of the force spectroscopy assay in which an AFM cantilever exerts force on the C-terminal tail of bR, causing an 8-amino-acid region (cyan) to reversibly unfold and refold between the fully folded conformation (I_G^0) and two partially unfolded intermediates (I_G^1, I_G^2). This behavior is seen in a plot of force vs. time (*Right*), which can be analyzed to give the unfolding free energy of the region.

imaging studies confirm the rotation of the F and E helices away from the C-terminal portion of the G helix in the open phase. However, none of these techniques quantify the energetic strengths of interactions formed and broken during the photocycle.

Recently, we developed AFM-based single-molecule force spectroscopy methods to measure membrane-protein energetics (31–34). These force spectroscopy studies overcome several key limitations of traditional chemical-denaturation assays; for example, our studies were performed in the native bilayer and were thus sensitive to specific protein–lipid interactions (34). In these studies, we site-specifically attached the C-terminal tail of bR to an AFM cantilever (35) and then used this cantilever to exert a force (F) that locally unfolded and refolded an 8-amino-acid (aa) region of the G-helix. In this region, three well-defined states were detected, starting from bR's fully folded state (Fig. 1*C*, cyan region of helix) (33, 35). Resolving these short lived, transiently occupied states—some with dwell times as short as ~10 μs and separated by ~1 nm—required focused-ion-beam (FIB) modified cantilevers that achieve a ~1-μs time resolution coupled with sub-pN stability over ~10 s (31, 35–37). We went on to demonstrate agreement between three distinct thermodynamic analyses that measured the unfolding free energy ΔG (33) of this 8-aa region, including an equilibrium analysis based on the inverse Boltzmann method (38). In subsequent work (34), we determined the change in unfolding free energy due to a single-amino-acid point mutation ($\Delta\Delta G_{mutant}$) and thus quantified the energetic contribution of that amino acid's side chain to overall protein stability.

Here, we measured a functionally important change in bR's internal energetics as it undergoes its photocycle. Specifically, we quantified the net change in the strength of all interactions between the C-terminal 8-aa region of the G helix—the same region discussed above—and the rest of the protein as the F and E helices rotate away from this terminal segment of the G helix during the open phase. We hypothesized that this energetic change would be destabilizing due to broken tertiary interactions between helices G and F (Fig. 1*B*). We triggered bR's photocycle with a brief light pulse (100 or 200 μs) while recording the equilibrium unfolding and refolding of this terminal 8-aa segment. A small percentage of individual records showed pronounced changes in this equilibrium due to photoactivation. Approximately 60% of these activated records showed the expected destabilization. In the other 40%, we observed a light-triggered, longer-lived putative "misfolded" state. For records that could be unambiguously assigned as exhibiting the expected destabilization, the photoexcitation durations were exponentially distributed with a lifetime of 38 ± 3 ms (fit ± uncertainty) in quantitative agreement with prior kinetic analysis from high-speed AFM imaging [33 ms (9)] and in concurrence with both the spectroscopic lifetime of state N (39) and time-resolved crystallography (7). The lifetime of this open phase increased with pH, as expected, and the frequency of activation dramatically decreased for the triple mutant D96G/F171C/F219L, which is thought to trap bR in its open phase (8, 40). Finally, equilibrium analysis based on the inverse Boltzmann method yielded a $\Delta\Delta G_{open}$ of 3.4 ± 0.3 kcal/mol (mean ± SEM). Thus, we demonstrated a force-spectroscopy approach for quantifying ligand-induced energetics and lifetimes of distinct functional states in a membrane protein by measuring modulations in local unfolding and refolding.

Results and Discussion

Detecting a Light-Induced Conformation Change in bR by Force Spectroscopy. To measure an energetic change in bR undergoing its photocycle, we started with an established AFM-based single-molecule force spectroscopy assay (33) and added a means to deliver precisely timed light pulses. In this established assay, bR embedded in its native lipid bilayer was sparsely labeled at its C terminus with dibenzocyclooctyne (DBCO), a copper-free click chemistry reagent (41), and deposited onto freshly cleaved mica. Next, an azide-functionalized, PEG-coated, FIB-modified cantilever was gently pressed into the sample to form a covalent linkage. At certain constant cantilever heights (Z), bR underwent rapid folding and unfolding between three states, its fully folded state and the first two unfolded intermediates, respectively, denoted I_G^0, I_G^1, and I_G^2 (Fig. 1*C*). I_G^2 represents unfolding of the terminal 8 amino acids of the G helix up to Lys^{216}, where the retinal is attached. This state is very mechanically robust, lasting over 60 s at 150 pN (35). The transition rates between the three states depend on F, and thus Z, as characterized in prior bR studies without photoactivation (33). Specifically, unfolding transition rates increase exponentially with F, while refolding transition rates decrease exponentially with F, as expected from the Bell model (42).

We achieved photoactivation by incorporating an ultra-thin 540-nm green light-emitting diode (LED) under the mica substrate (Fig. 2*A*). This LED was connected to the AFM controller using a home-made circuit that provides for precise delivery of short light pulses synchronized with AFM data acquisition. We primarily used 200-μs light pulses, which resulted in an estimated force error of 1 pN due to heating of the mica (*SI Appendix*, Fig. S1). A pH 7.8 buffer was used in our initial studies to compare with our prior AFM results (33, 34). Data at higher pH are presented in a subsequent section.

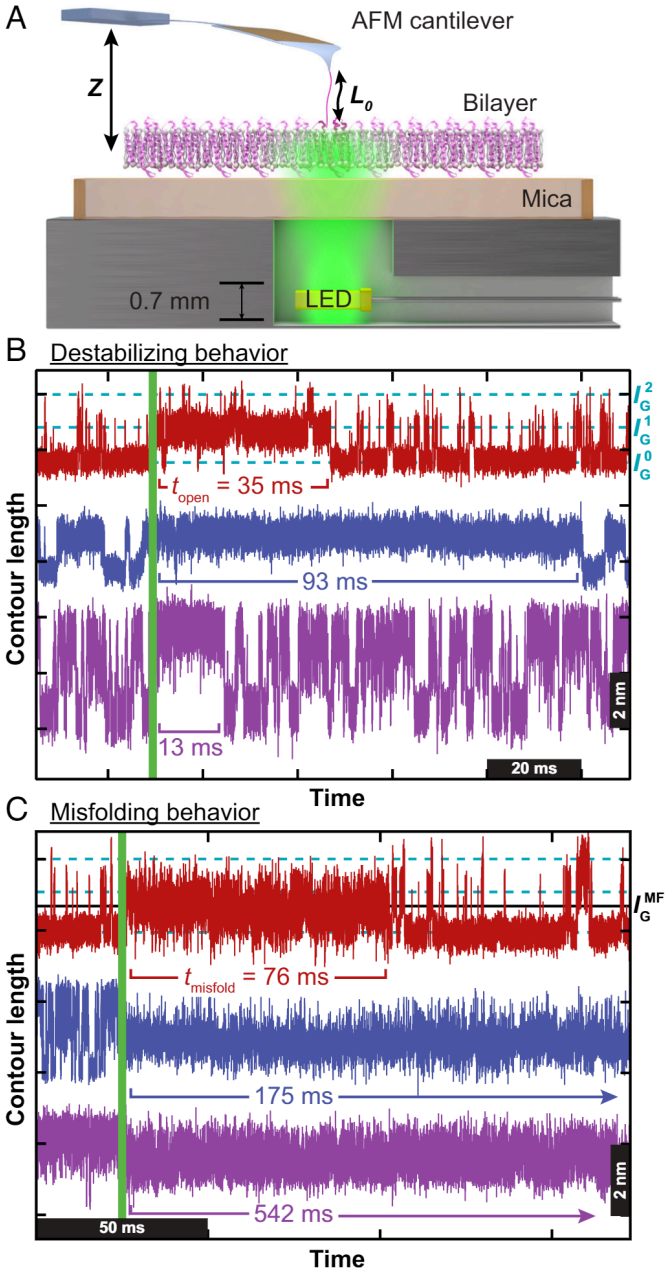

Fig. 2. Photoactivation of a single molecule of bR (*A*) Diagram of the experimental setup (not to scale). After formation of a linkage between bR embedded in its native lipid bilayer and the AFM cantilever, the cantilever is retracted to a height *Z* above the sample. Thermal motion drives transitions between folded and partially unfolded states in helix G (e.g., Fig. 1*C*), each characterized by a different contour length of unfolded polypeptide chain (L_0). A thin LED beneath the mica illuminates the bR with a 200-μs light pulse (vertical green line, not to scale) during each dwell at constant *Z*. (*B* and *C*) Three L_0-vs-time traces from different molecules at varying *Z* (and therefore *F*) illustrating the expected destabilizing behavior (*B*) and previously undescribed misfolding behavior (*C*). The duration of this photoexcitation is denoted t_{open} or $t_{misfold}$, respectively. Dashed horizontal lines denote the three states expected from Fig. 1*C*; the solid black line denotes I_G^{MF}. Note, the vertical order of I_G^0, I_G^1, and I_G^2 are reversed in a plot of L_0 relative to a plot of force (Fig. 1*C*). Also, the misfolded phase in the two bottom traces last longer than the portion of the record shown. Data collected at 5 MHz and downsampled to 200 kHz.

To efficiently detect multiple light-induced conformational changes per bR molecule, we used a more sophisticated data-acquisition procedure than the typical constant-velocity pulling assay used in AFM studies (*SI Appendix*, Fig. S2). To initiate the assay, we gently touched the azide-functionalized cantilever to the DBCO-labeled bR, then retracted the cantilever at 300-nm/s velocity until reaching 150 pN of tension. This elevated force indicated that a bond had formed between the tip and sample, triggering the rest of the acquisition procedure. The cantilever was then slowly moved back into soft contact with the surface. This slow approach allowed us to estimate the Z value at which three-state folding/unfolding behavior occurred (Fig. 1*C*) by analyzing the variance in *F*, since this variance increased during near-equilibrium folding between I_G^0, I_G^1, and I_G^2 (*SI Appendix*, Fig. S2*C*). We then moved the cantilever through a series of constant-*Z* positions centered around this value, dwelling at each *Z* for 200 ms. We digitized the cantilever deflection, and therefore *F*, at 5 MHz. We recorded data without illumination for the first 50 ms of each dwell to establish baseline three-state folding/unfolding behavior. We then pulsed the green LED for 200 μs and observed the effect for a further 150 ms before moving to the next *Z* position. bR was photoactivated ~10% of the time following 200-μs illumination, as evidenced by an altered occupancy in the three states. For each bR molecule, we performed a total of 60 200-ms cycles over 20 different cantilever heights bracketing the three-state transition force. Importantly, photoactivation efficiency increased with pulse duration [5.7 ± 1.2% at 100 μs (N = 420 pulses) and 9.9 ± 0.7% at 200 μs (N = 2,280)], consistent with these events arising specifically from photoexcitation. Moreover, photoactivation occurred from all three states (I_G^0, I_G^1, and I_G^2).

We observed behavior consistent with the expected open-phase destabilization of the G helix by loss of contacts with the F helix in ~60% of photoactivation events (Fig. 2*B*). In these events, there was an abrupt change in the occupancy between I_G^0, I_G^1, and I_G^2 after a short lag time following illumination [t_{lag} = 5 ± 2 ms (mean ± SEM)]. This destabilization led to increased occupancy of the more extended unfolded states, I_G^1 and I_G^2. This perturbed phase persisted with an exponential lifetime of τ_{open} = 38 ± 3 ms (fit ± uncertainty) before abruptly returning to the original population distribution (see below for details of kinetic analysis).

In the other ~40% of the photoactivated events, we observed an unexpected phenomenon illustrated in Fig. 2*C*. These events had a shorter average t_{lag} < 1 ms and remained in the perturbed phase much longer ($\tau_{misfold}$ = 139 ± 2 ms). In these events, the light-induced change in the probability distribution was not uniformly destabilizing, and the transitions were no longer exclusively between the three well-defined states I_G^0, I_G^1, and I_G^2. Rather, these examples of photoexcitation promoted occupancy of a putative misfolded state I_G^{MF} between I_G^0 and I_G^1, even when I_G^2 was primarily occupied before illumination.

These two behaviors, which we refer to as G-helix destabilization and misfolding, respectively, can be distinguished by two metrics. The first metric is based on differing effects on the underlying energy landscape governing transitions in this 8-amino-acid region. Destabilization promotes occupancy of more-unfolded conformations, whereas the misfolding behavior promotes a new minimum at I_G^{MF}. Using this metric, we could distinguish G-helix destabilization from misfolding in 57% of records, but the other 43% were ambiguous. This metric was biased, in that it was more successful in identifying misfolding than destabilization. The second metric is based on the differing characteristic exponential time constants of the two behaviors (38 vs. 139 ms; see below). Because the transition from the open to the closed phase was stochastic, these time constants could not be used to uniquely assign individual records to one behavior or the other. But, importantly, they could be used to make an unbiased determination of the relative

frequencies of the two behaviors in the entire dataset. Moreover, these two behaviors appear to be distinct as we have no records where we saw interconversion of a photoactivated molecule between them. And, the same individual molecule can exhibit both behaviors during separate photoactivations. In the following sections, we explore the energetic consequences of both the destabilizing and misfolded behaviors, then discuss the pH-dependent kinetics of each, and conclude by studying a triple mutant that traps bR in its open phase.

Measuring a $\Delta\Delta G$ between Open and Closed Phases of the Photocycle. The loss of contacts between the G and F helices due to the rotation of the F and E helices destabilizes the terminal 8 amino acids of the G helix during the open phase. We quantified the total open-phase destabilization of this region relative to the closed phase ($\Delta\Delta G_{\text{open}}$) by analyzing traces similar to Fig. 2*B*.

We first plotted the constant-Z data in terms of contour length (L_0) (Fig. 3*A*) so that each folding state corresponded to a particular L_0 regardless of F. Here, L_0 is the contour length of unstructured amino acids under tension, which can be related to the number of amino acids unfolded via the contour length of each amino acid [0.366 nm/aa (31)] and the helix geometry from bR's known structure (24). Each 200-ms constant-Z segment was then divided into two phases: the photoexcited, open phase (*purple*), which followed the light pulse, and the unexcited, closed phase (*gray*), which constituted the rest of the trace (Fig. 3*A*). In each phase, we histogrammed the amount of time the protein spent at each value of L_0. Analysis of this probability distribution yielded a 1-dimensional (1D) energy landscape for the three states, reconstructed using the inverse Boltzmann method where the natural logarithm of that phase's probability distribution is multiplied by $-k_B T$. To compare landscapes, we aligned them at I_G^2, used here as the standard reference state in which all stabilizing interactions of the 8-aa region are disrupted by applied force. Comparison of the aligned landscapes shows the energetic differences between the open and closed phases (Fig. 3*B*). It is important to note that features on these experimentally derived landscapes are broadened by the compliance of the AFM cantilever and the taut, unstructured polypeptide (38); however, this analysis only requires the energy differences between the states ($\Delta\Delta G_{\text{open}}$) and is not compromised by such broadening in our assay.

In some cases, $\Delta\Delta G_{\text{open}}$ can be obtained directly from these reconstructed free-energy landscapes as the difference of ΔG values in the two phases (open phase denoted with *):

$$\begin{aligned}\Delta\Delta G_{\text{open}} &= \Delta G - \Delta G^*, \\ &= [G(I_G^0) - G(I_G^2)] - [G^*(I_G^0) - G^*(I_G^2)], \\ &= G(I_G^0) - G^*(I_G^0). \end{aligned} \quad [1]$$

The final line is true because $G(I_G^2) = G^*(I_G^2) = 0$ by use of I_G^2 as the standard reference state. We note that $\Delta\Delta G_{\text{open}}$ shown in Fig. 3*B* was determined when the bR was under tension. Recovery of zero-force ΔG values requires subtraction of the works done to bend the cantilever, to stretch the linker, and to stretch the amino acids liberated by unfolding (33). Importantly, however, all of these corrections are common between the open and closed phases, since the locations of I_G^0 and I_G^2 did not change upon photoexcitation. Thus, $\Delta\Delta G_{\text{open}}$ can be determined as the difference between the open- and closed-phase energy landscapes at I_G^0, the fully folded state (Fig. 3*B*). The ability to arrive at this value without the introduction of any potential systematic error from calculation of the large correction factors mentioned above

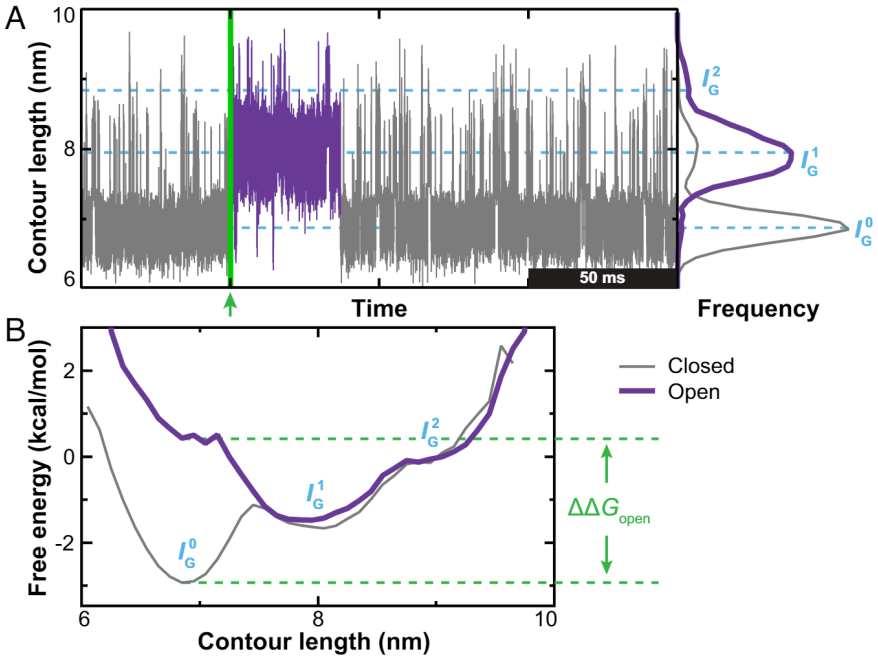

Fig. 3. Determining $\Delta\Delta G_{\text{open}}$ using the inverse Boltzmann method. (*A*) A plot of L_0 vs. time at a particular cantilever Z value divided into the closed phase (gray) and photoexcited open phase (purple) following the light pulse (vertical green line above arrow). Histograms (*Right*) show the relative occupancy of each L_0 value in each phase. (*B*) A reconstructed 1D free-energy landscape of the 8-amino-acid region of interest calculated by multiplying the logarithm of the relevant population by $-k_B T$. The free energy was set to 0 at I_G^2, used here as the standard reference state. The overall $\Delta\Delta G_{\text{open}}$ for the 8-amino-acid region is then given by the difference in free energy at I_G^0 (dashed green lines). Note, the relative spacing between intermediates remains constant but the absolute value of L_0 varies between molecules due to polydispersity in PEG length.

Table 1. Photoisomerization-induced destabilizing free-energy changes

	$\Delta\Delta G_{open}$ (kcal/mol)		
Transition	Total	Per amino acid	*N*
$I_G^0 \leftrightarrow I_G^1$	−2.7 ± 0.2	0.5	9
$I_G^1 \leftrightarrow I_G^2$	−0.7 ± 0.2	0.2	10
$I_G^0 \leftrightarrow I_G^2$	−3.4 ± 0.3	0.4	Note*

*Values reported are the sums of the values for the two constituent transitions.

motivated our use of the inverse Boltzmann analysis in this work. We stress, however, that our prior study of the energetics of this region of bR in the absence of light pulses established agreement between this inverse Boltzmann approach, a kinetics-based analysis, and an application of the Crooks fluctuation theorem (33). For the data shown in Fig. 3, analysis according to Eq. **1** yielded $\Delta\Delta G_{open}$ = −3.1 kcal/mol (−5.3 k_BT) and visually highlights how the primary difference between the open and closed phases was the decreased stability of I_G^0, with a smaller change in I_G^1.

In practice, we computed $\Delta\Delta G_{open}$ treating the $I_G^0 \leftrightarrow I_G^1$ and $I_G^1 \leftrightarrow I_G^2$ transitions separately since most events did not exhibit transitions between all three states in both the closed and open phases. To do so, we first fit the probability distribution for each phase to a set of Gaussians to determine the probability P_i of occupying state *i* and then used the inverse Boltzmann expression given by

$$\Delta G_{ij} = -k_B T \ln\left(\frac{P_j}{P_i}\right), \quad [2]$$

where ΔG_{ij} is the difference in free-energy between two states *i* and *j*. Eq. **1** was sequentially applied to each two-state transition separately (*Materials and Methods* and *SI Appendix*, Fig. S3). Free energy results for each transition (i.e., $\Delta\Delta G_{open}^{01}$, $\Delta\Delta G_{open}^{12}$) are given in Table 1 with the scatter between individual measurements plotted in *SI Appendix*, Fig. S4. Combining these results between events yielded an overall average $\Delta\Delta G_{open}$ of −3.4 ± 0.3 kcal/mol (mean ± SEM). In combining $\Delta\Delta G_{open}$ values obtained from records at different *Z* (and thus *F*), we assume that $\Delta\Delta G_{open}$ is not force dependent or, in other words, that the effect of force is to perturb the equilibrium between conformational states but not to alter the energy landscape beyond what is predicted by the Bell model (42). This assumption is consistent with multiple observations about the 8-amino-acid, three-state region under study in the closed phase. First, our previous measurement of the exponential dependence of transition rates on *F* between the these states implies an energetic dependence on *F* fully explained by the Bell model (42). Additionally, the observed unfolding contour-length changes between states are consistent with expectations from the unperturbed structure (35). Furthermore, we see no discernable force dependence in the individual $\Delta\Delta G_{open}$ values of the present study (SI *Appendix*, Fig. S4).

Interpreting $\Delta\Delta G_{open}$ in the Context of Prior Studies. The known bR crystal structures (7) suggest that secondary structure is undisturbed in the open phase of the photocycle, but that tertiary interactions are disrupted by the rotation of helices E and F. Disrupted interactions will decrease the unfolding free energy of the residues that had previously participated in them. In particular, when the F helix undergoes its light-induced rotation (7), the C-terminal 8 amino acids of the G helix lose multiple contacts with the F helix, particularly G-helix residues Phe[219], Ile[222], and Leu[223]. This results in the lower unfolding free energy of the photoexcited, open phase and therefore the measured negative $\Delta\Delta G_{open}$.

The magnitude of $\Delta\Delta G_{open}$—a quantity not accessible in prior measurements—is consistent with a ~1 to 2 kcal/mol energetic cost to break side-chain:side-chain tertiary interactions in the lipid bilayer. Prior chemical-denaturation (43–48) and AFM-based force spectroscopy (34) studies have typically found $\Delta\Delta G_{mutant}$ values of 0.5 to 2.5 kcal/mol when an amino acid is replaced with alanine in bR. These $\Delta\Delta G_{mutant}$ values are interpreted as the energetic contribution of the mutated side chain to the overall stability of the protein.

We can make a simplistic estimate of $\Delta\Delta G_{open}$ based on the known crystal structures of the open and closed phases of bR. The closed-phase structure shows that Leu[223] in the G helix contacts Thr[170] and Leu[174] of the F helix; Ile[222] in the G helix contacts Thr[170], Val[173], Leu[174], and Val[177] of the F helix; and Phe[219] in the G helix contacts Leu[174], Val[177], and Thr[178] of the F helix (as well as a structured water) (49). The open-phase structure shows that the light-driven rotation of the F helix breaks the two Leu[223] contacts, three of the four Ile[222] contacts, and one of the three Phe[219] contacts (7) (illustrated in *SI Appendix*, Fig. S5). If all interhelical contacts of a given residue were broken, we can estimate the effect on $\Delta\Delta G_{open}$ to be equal to the single-amino-acid alanine mutation $\Delta\Delta G_{mutant}$ value. The value of $\Delta\Delta G_{mutant}$ for Leu[223] has been measured by both chemical denaturation [−2.1 ± 0.1 kcal/mol (47)] and by us using AFM-based force spectroscopy [−2.3 ± 0.6 kcal/mol (34)]. The value of $\Delta\Delta G_{mutant}$ for Ile[222] has been measured by chemical denaturation as −0.9 ± 0.2 kcal/mol. Combining the values for these two residues and scaling the Ile[222] value by ¾ (to account for its one surviving F-helix contact) gives our estimate of −2.8 kcal/mol for the $I_G^0 \leftrightarrow I_G^1$ transition.

This rough estimate of −2.8 kcal/mol is very close to our measured $\Delta\Delta G_{open}^{01}$ value of −2.7 ± 0.2 kcal/mol for the transition in which these residues unfold (Table 1). The contribution of Phe[219], which is the only F-helix-contacting residue that unfolds during the $I_G^1 \rightarrow I_G^2$ transition, is harder to estimate from prior studies, since multiple attempts to mutate that residue have resulted in uninterpretable chemical-denaturation results (47, 48). Here, we measured $\Delta\Delta G_{open}^{12}$ = −0.7 ± 0.2 kcal/mol. Given that this value arises from breaking just one of the three interhelical contacts of Phe[219], it is reasonable to expect that breaking all three of them—as occurs in a mutation study—might have a sufficiently large and non-local energetic effect to explain the failure of chemical-denaturation measurements. The greater number of broken tertiary contacts in $I_G^0 \rightarrow I_G^1$ versus in $I_G^1 \rightarrow I_G^2$, which occurs because of the rotation of the F helix (Fig. 1*B*), explains why $\left|\Delta\Delta G_{open}^{01}\right| < \left|\Delta\Delta G_{open}^{12}\right|$ on both absolute and per-amino-acid bases.

Characterizing Misfolding Behavior. In addition to the G-helix destabilizing behavior discussed above, we also observed light-induced misfolding that *stabilized* a distinct state between I_G^0 and I_G^1, denoted I_G^{MF} (Fig. 4*A*), and that persisted with an exponential lifetime of 139 ± 2 ms at pH 7.8. The exact location of I_G^{MF} is trimodally distributed with peaks at contour lengths equal to 40, 60, and 80% of the separation between states I_G^0 and I_G^1 (Fig. 4*B*). Under the assumption that misfolding does not lead to a significant structural rearrangement, these contour length changes

correspond to unfolding up to residues Ile^{222}, Leu^{221}, or Gly^{220}, respectively. The energy landscape of the misfolded phase (Fig. 4*C*) differs qualitatively from both the closed and open phases of G-helix destabilization (Fig. 3*B*) as I_G^{MF} is strongly stabilized with respect to all other states. The stabilization of I_G^{MF} with respect to the closed-phase I_G^1 is 2.7 ± 0.2 kcal/mol (SEM, N = 24); although, the very high occupancy of I_G^{MF} in the misfolded phase relative to I_G^2 as the reference state likely introduces systematic artifacts into this value (scatter of values and details of calculation given in *SI Appendix*, Fig. S6). This distinctive energy landscape provided criteria for rigorously identifying misfolding, either by noting a stabilization of I_G^{MF} with respect to I_G^2 or by noting a significant shift in the location of I_G^{MF} compared to that of I_G^1.

This misfolding behavior was unexpected in two ways. First, the observation that a more-folded state would be stabilized with respect to the standard state I_G^2, as in Fig. 4*C*, is inconsistent with the picture of interhelical interactions being disrupted by the light-induced rotation of the F helix seen in time-resolved crystallography experiments (7) (Fig. 1*B*). Second, the 139-ms lifetime of this phase is dramatically longer than the ~10- to 30-ms lifetimes reported by spectroscopy, time-resolved crystallography, and high-speed AFM imaging (7, 9, 39). In particular, the open-phase dwell times reported in the high-speed AFM imaging study of Perrino et al. (9), in which no pulling forces were applied, were well fit by a single exponential (τ = 33 ms) without an appreciable tail extending above 100 ms.

Interestingly, we have previously seen misfolding but at a much rarer frequency in similar non-photoactivated studies of bR. Reviewing the raw data of Yu et al. (33), in which bR was treated with a protocol of constant-Z dwells similar to the present work but without light pulses, we found a total of five instances of misfolding spread across 58 200-ms dwells exhibiting $I_G^0 \leftrightarrow I_G^1$ transitions (examples shown in *SI Appendix*, Fig. S7). This constitutes a misfolding probability of 0.2% in any 5-ms window, compared with a 6% probability of misfolding under the same $I_G^0 \leftrightarrow I_G^1$ conditions in the 5 ms after a 200-μs light pulse of the present study. Hence, misfolding competes with our three well-defined states (I_G^0, I_G^1, and I_G^2) but becomes 30-fold more likely to occur immediately after illumination. A kinetic rate diagram encoding this idea by making certain transition rates light-pulse-timing dependent is sketched in *SI Appendix*, Fig. S8.

Misfolding persisted under several variations in the experimental procedure. We hypothesized that either mechanical force applied to the G helix and/or partial unfolding up to I_G^1 or I_G^2 during photoactivation might promote misfolding. To test these hypotheses, we performed a modified assay in which we dropped the tension to zero for 5 ms before triggering the light pulse and then restored the cantilever to its original Z position at 5 ms after illumination (*SI Appendix*, Fig. S9). This 5-ms delay after the light pulse precluded measuring t_{lag} but still allowed us to observe photoexcitation behavior for all but the shortest open- or misfolded-phase durations. We observed misfolding events in 42 ± 13% of these force-drop records, as determined using the energy-landscape criteria above, vs. 39 ± 9% in the standard assay using the same criteria (uncertainties are $\sqrt{N}$ error of counting statistics). Thus, we concluded that tension in the G helix and/or partial unfolding at the moment of photoexcitation do not explain the misfolding behavior. We also hypothesized that misfolding might arise due to

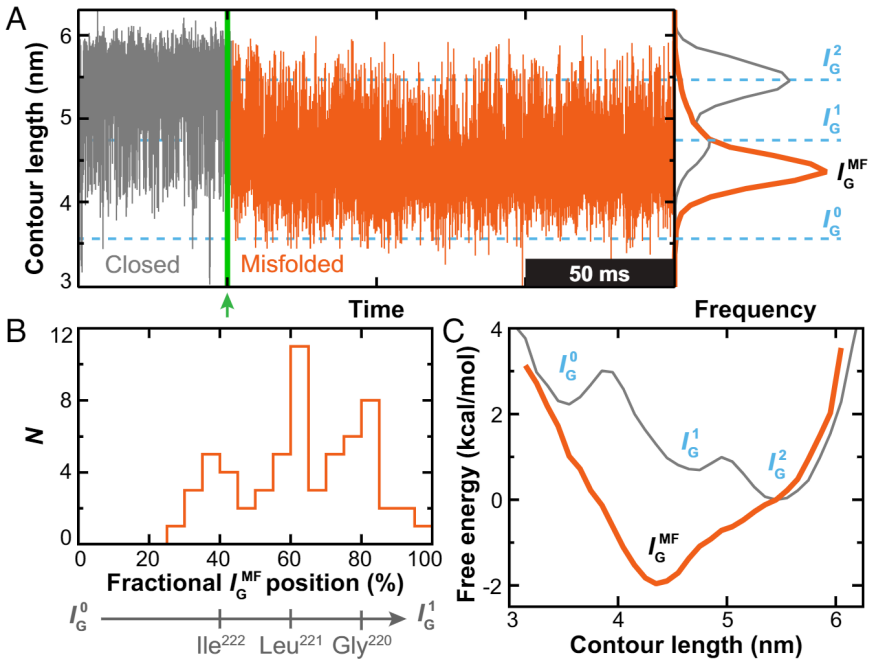

Fig. 4. Characterization of misfolding behavior. (*A*) A plot of L_0 vs. time showing bR entering a single long-livid, photoexcited, misfolded phase (orange) after a 200-μs photoexcitation (green arrow). Histograms of each phase show the peak location (I_G^{MF}) of the misfolded state does not align with the three well-established states (dashed cyan) seen in the closed phase (gray). (*B*) Histogram of I_G^{MF} location (peak of single-molecule histogram) across 63 analyzed records, expressed as a percentage of the total contour-length difference between established states I_G^0 and I_G^1. The peaks of the trimodal distribution correspond to unfolding up to three different amino acids in helix G (*below*). (*C*) Reconstructed free-energy landscapes derived from inverse Boltzmann method (Eq. **2**) of both closed- (gray) and open-phase (orange) data of panel *A*, highlighting the energetic stability of misfolded state I_G^{MF} relative to I_G^2, even though I_G^2 was the most populated state prior to illumination.

the interaction of two photoexcited bR molecules in the purple-membrane trimer lattice. To test this, we reduced our light pulse duration by a factor of two, which was expected to reduce the chance of a pair of molecules both being photoexcited by a factor of four. At a reduced 100-μs pulse duration, we saw 57 ± 16% misfolding events, roughly consistent with the results at 200 μs despite the larger error due to the lower efficiency in photoactivation (N = 13 unambiguous misfolding events, out of 23 total). Finally, the misfolding fraction did not depend on pH: 39 ± 9% misfolding at pH 7.8 versus 34 ± 5% at pH 9.5.

Absent the obvious hypothesis that misfolding arises from our application of force, which we rejected based on the force-drop assay discussed immediately above, we are left with the possibilities that *i*) misfolding may be a more-subtle consequence of the force-spectroscopy assay or *ii*), speculatively, misfolding may represent a process off of the canonical photocycle pathway that is detectable in our assay but not in prior studies. Even though force or partial unfolding of the G helix is not required for misfolding, it may be that the photocycle conformational changes of the rest of the protein sufficiently alter the environment of the G helix that it can sometimes adopt this alternate configuration. The misfolded configuration, however, involves *stabilization* of the majority of the 8 amino acids at the C terminus of the G helix; it is not obvious how such stabilization would arise if the F helix had rotated away, breaking tertiary contacts. This motivates an alternative explanation that the canonical rotation of the F and E helices may not have occurred during misfolding despite photoactivation. It is conceivable that such a situation, even if it routinely occurred during the photocycle, would be invisible to other assays that are not directly sensitive to the energetics of the contacts between helices G and F. For example, the high-speed AFM imaging studies of Perrino et al. (9) monitor the movement of the E-F loop, which would not occur if helices E and F do not rotate. Likewise, the time-resolved crystallography studies require the deconvolution of multiple coexisting subspecies and may not have the power to resolve three additional, sparsely populated misfolded states (Fig. 4*B*).

Destabilization and Misfolding Kinetics and their pH Dependence. During the open phase of the photocycle, a proton is transferred from Asp^{96} to the Schiff base connecting Lys^{216} to the retinal via a chain of three crystallographically resolved water molecules (Fig. 5*A*, light-green arrows) (7). The open phase ends when Asp^{96} is reprotonated by a bulk proton from the cytoplasm (Fig. 5*A*, dark-green arrow). In the spectroscopic nomenclature, these proton transfers correspond to the M→N and N→O transitions, respectively (50). The kinetics of this latter step is dependent on the bulk concentration [H^+] and is therefore expected to become slower with increasing pH. This pH-dependent kinetics is seen in multiple prior studies (14, 51). Hence, we sought to quantify the kinetics of photoexcited bR as function of pH to compare with prior results and confirm a pH-dependent lifetime of the open phase.

Our photoactivated events were characterized by two timescales: a short lag time between the light pulse and the start of perturbed behavior (t_{lag}) and the longer-duration photoexcitation (t_{open} or $t_{misfold}$). The start and end points of the photoexcitation were identified by eye using the abrupt change in dynamics upon excitation (e.g., Fig. 2 *B* and *C*). Our approximate resolution in determining these times was ~1 ms and was set by the lifetimes of I_G^0, I_G^1, and I_G^2 (i.e., the timescale over which the protein samples its energy landscape). The transition rates between I_G^0, I_G^1, and I_G^2 are on the scale of $5 \times 10^3\ s^{-1}$ (33), corresponding to state lifetimes on the ms timescale. Thus, our assay is better suited to characterizing photoexcited

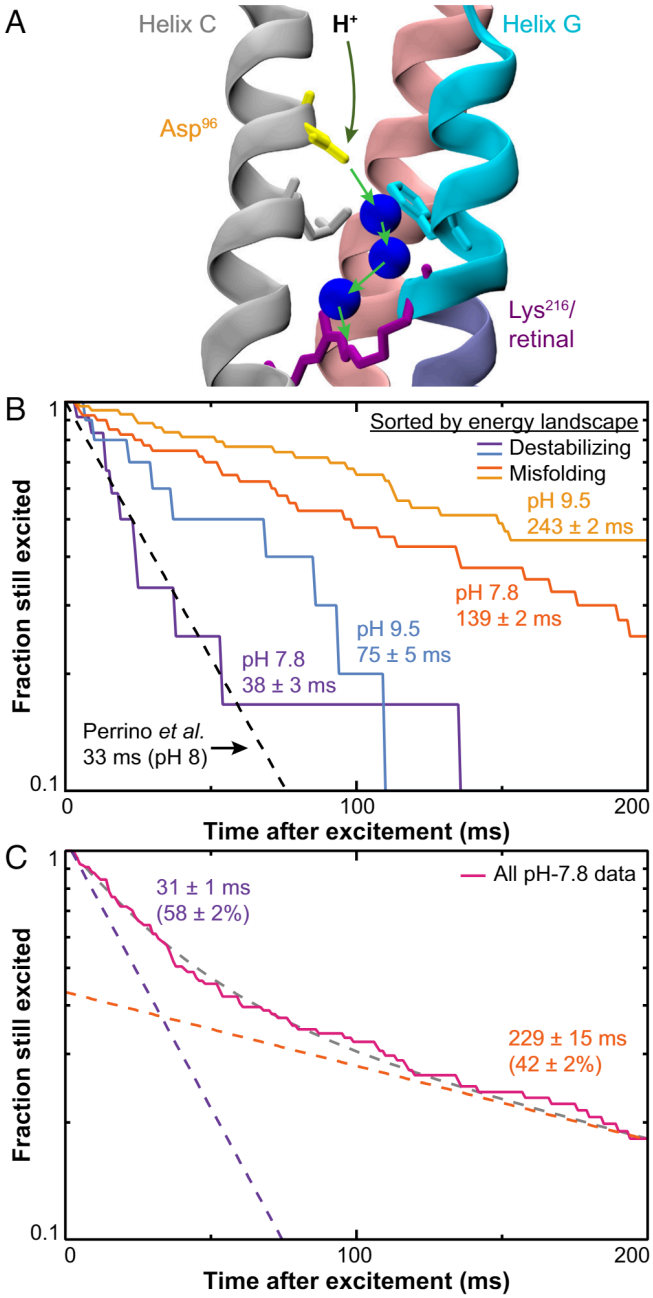

Fig. 5. Kinetics of destabilization and misfolding events are modulated by pH. (*A*) Rendering of the crystal structure of the open phase [(7), PDB: 6RPH] with arrows illustrating the proton-transfer path. First, a proton is transferred from Asp^{96} to the Schiff base connecting Lys^{216} to the retinal (green arrows) via three waters (blue). Then, Asp^{96} is reprotonated by a bulk proton from the cytoplasm at a rate that depends on pH (dark green arrow). (*B*) Plots of the survival probability distribution of observing a molecule that remains in the photoexcited phase longer than a specified time, at two pH values. Energy landscape criteria were used to separate destabilizing and misfolding behavior with only unambiguous traces plotted. Single-exponential fits yielded the time constants shown. Also plotted is the decay expected from the 33-ms time constant found in the AFM imaging experiments of Perrino et al. (9) at pH 8 (dashed black). (*C*) Survival probability distribution plot of *all* pH-7.8 data (N = 121) was well described by a double exponential with the two time constants and two amplitudes of each decay path shown.

phase lifetimes, which occur on ~10- to 100-ms timescales, rather than the much-shorter t_{lag}.

The energy-landscape sorting criteria, as described above, can rigorously classify *some* of the photoexcited events into destabilization (t_{open}) or misfolding ($t_{misfold}$) phenomena. From this subset of data, we separately computed the complementary cumulative

(survival) probability distribution for observing a phase duration longer than a specified time for the destabilized and misfolded molecules (Fig. 5*B*). The resulting plots are approximately linear on semi-log axes, showing destabilization and misfolding events were exponentially distributed. We analyzed the data using $\exp(-t/\tau)$, where τ is the time constant. Fits were weighted by the number of molecules represented by each data point and uncertainties were taken as the one-sigma confidence intervals of these fits. At pH 7.8, these fits yielded $\tau_{\text{open}} = 38 \pm 3$ ms for the destabilizing behavior and $\tau_{\text{misfold}} = 139 \pm 2$ ms for the misfolding behavior.

Our value for τ_{open} is in quantitative agreement with the 33-ms value from high-speed AFM imaging experiments at pH 8 (Fig. 5*B*, dashed line) (9). This agreement with a study based on surface topography provides increased confidence in our assignment of G-helix destabilization to the open phase, our method of distinguishing destabilization from misfolding, and that application of substantial mechanical force to the G-helix did not significantly alter bR's photocycle properties.

We next quantified bR photoactivation at elevated pH (9.5), using the same energy-landscape criteria to assign a fraction of events as exhibiting either the destabilization or misfolding phenomenon. For these unambiguous cases, we again plotted the survival probability distribution for each phenomenon as a function of duration (Fig. 5*B*). For the destabilizing behavior, we saw a twofold increase in τ_{open} from 38 ± 3 ms at pH 7.8 to 75 ± 5 ms at pH 9.5, consistent with the structural insight that reduced bulk proton concentration would slow the reprotonation of Asp[96]. We note that bR does not have cysteine or histidine in its structure that would experience differing protonation at this elevated pH. This twofold change in τ_{open} is smaller than that seen in the prior spectroscopic studies but larger than in the high-speed AFM imaging study. Specifically, absorption spectroscopy work reported a sevenfold increase in τ from pH 8 to 9 (14) and Raman spectroscopy work reported a fivefold increase in τ from pH 8 to 8.6 (51). However, the high-speed AFM imaging study showed minimal change in kinetics from pH 8 to 9. We note that this imaging study did observe an increased lifetime when pH was increased from 7 to 8 (τ = 14 vs. 33 ms, respectively) (9).

Interestingly, misfolding kinetics were also pH dependent, with τ_{misfold} increasing 1.7-fold from pH 7.8 to 9.5. Quantitatively, τ_{misfold} increased from 139 ± 2 ms to 243 ± 2 ms (Fig. 5*B*). This pH dependence suggests that reprotonation is also involved in the transition from the misfolded photoexcited phase back to the unexcited phase of bR and that misfolded molecules could still possibly pump protons.

When the lifetimes of *all* the photoexcited events for each pH were analyzed (i.e., not just those that could be distinguished by their energy landscapes), the two distinct time scales associated with G-helix destabilization and misfolding were also observed. To quantify the data, we again plotted the normalized survival lifetime distributions (Fig. 5*C*). These data were well modeled by the sum of two exponentials: $A_{\text{open}} \exp(-t/\tau_{\text{open}}) + A_{\text{misfold}} \exp(-t/\tau_{\text{misfold}})$, where A represents the amplitude. At pH 7.8, the resulting values were $\tau_{\text{open}} = 31 \pm 1$ ms and $\tau_{\text{misfold}} = 229 \pm 15$ ms, which exhibit an order-of-magnitude separation similar to the values of 38 ms and 139 ms seen in the sorted data, respectively. The amplitudes yielded an unbiased measure of the frequency of the two behaviors: $A_{\text{open}} = 58 \pm 2\%$ and $A_{\text{misfold}} = 42 \pm 2\%$. We also performed this analysis for all pH-9.5 data (*SI Appendix*, Fig. S10), which showed a 2.1-fold increase in τ_{open} and a 1.7-fold increase in τ_{misold}, both results consistent with the sorted data. Thus, the observation of distinct destabilization and misfolding phenomena with different photoexcited lifetimes was not an artifact of the energy-landscape criteria used to select for unambiguous cases of open and misfolded events.

Triple Mutant (D96G/F171C/F219L) Significantly Reduces Photoactivation Efficiency. The bR triple mutant D96G/F171C/F219L is thought to trap bR in its photoexcited "open" phase, even in the absence of illumination (8, 40). We hypothesized that this triple mutant would not show photoactivation in our assay, since the G helix would already be destabilized due to the decreased tertiary interactions between helices G and F.

To test this hypothesis, we tried to photoactivate the triple mutant at pH 7.8 with 200 μs light pulses. Over six molecules, each subject to 60 light pulses, we observed six photoactivation events of any kind (i.e., destabilizing, misfolding, or ambiguous); the mutant otherwise exhibited dynamics between states I_G^0, I_G^1, and I_G^2 similar to the wild type, but without any light-dependent effect (*SI Appendix*, Fig. S11). This represents a photoactivation efficiency of 1.7 ± 0.7% per light pulse (uncertainty from counting statistics) versus a rate of 9.9 ± 0.7% in wild-type bR studied. This 5.8-fold reduction was statistically significant ($P < 1 \times 10^{-5}$ in a two-tailed Z test). Thus, the triple mutant is much less likely to exhibit photoactivation, as expected from its structure where the F and E helices are already in the open conformation regardless of photoexcitation (40).

That the triple mutant remains in an "open-like" configuration is seen by calculating the difference in unfolding free energy of the 8-amino-acid region between the triple mutant and the wild-type results previously reported (33): $\Delta\Delta G_{\text{TM}} = \Delta G_{\text{u}}^{\text{TM}} - \Delta G_{\text{u}}^{\text{WT}} = -6.9 \pm 1.3$ kcal/mol. Here $\Delta G_{\text{u}}^{\text{TM}}$ was calculated using the inverse Boltzmann method with appropriate corrections, as in prior work (33). That the value is less than 0 confirms that the triple mutant is destabilized with respect to the wild type. That the value is significantly larger than the $\Delta\Delta G_{\text{open}} = 3.4 \pm 0.3$ kcal/mol discussed above, and also that there is apparent heterogeneity in the relative contributions of the $I_G^0 \leftrightarrow I_G^1$ and $I_G^1 \leftrightarrow I_G^2$ transitions, suggests a more-complicated triple-mutant behavior, the characterization of which is beyond the scope of the present work.

The decreased rate of photoactivation and the occupancy of an open-like state (based on $\Delta\Delta G_{\text{TM}}$) in the triple mutant both add further evidence to our interpretation of photoactivation events in wild-type bR as arising from photocycle conformational changes, since they are suppressed in a mutant that does not exhibit the changes. We note, though, that photoactivation was not entirely suppressed in the triple mutant, which could be due to some degree of residual conformational change [as in the electron difference maps of Subramaniam et al. (8)] or a perturbation of the triple-mutant conformation under applied force. Further study of these possibilities awaits technical advances that enable assays with much larger data sets needed to compensate for the rarity of triple-mutant photoactivation.

Conclusions

In this work, we developed an assay to measure the energetics associated with a ligand-induced conformational change of a membrane protein in its native lipid bilayer using AFM-based single-molecule force spectroscopy. Photoactivation of bR's ligand retinal using sub-ms pulses of light occurred stochastically and at a relatively low frequency that increased with light-pulse duration but was greatly reduced in a conformationally trapped triple mutant. Hence, the observed photoactivation was not a simple heat-induced artifact. Moreover, bR entered the open phase in ~60% of these photoactivation events, as evidenced by G-helix

destabilization, kinetics consistent with prior work, and the expected increased lifetime at higher pH. Such concurrence with expected open-phase physiological properties is perhaps surprising given the AFM applied ~100 pN force to the C-terminal tail and, at times, unfolded up to Lys^{216}, where the retinal is bound. Yet, bR could nonetheless complete its photocycle. Our success thus provides support for the general strategy of these measurements: using the equilibrium unfolding and refolding of a small portion (8 aa) of the G helix to report on the strength and lifetime of tertiary interactions with other parts of the protein that are undergoing ligand-induced conformational changes without globally unfolding the protein. Future studies could use loop scission between pairs of transmembrane helices (52, 53) coupled with attachment at non-terminal peptide locations to map out the perturbed energetics of the rotated EF helix pair with other parts of bR. This work also establishes a more general approach for measuring ligand-induced energetic changes in other membrane proteins, either due to ligand isomerization (as in this case, modulated by light) or ligand binding (modulated by bulk concentration).

Materials and Methods

Sample Preparation. We prepared DBCO-labeled bR starting from the S248C bR mutant as in prior work (35). Briefly, the bR was expressed using a plasmid-based platform in *H. salinarum* (45), purple membrane was extracted using an established protocol (54), and the bR in the membrane was sparsely (~1%) labeled at the engineered cysteine residue by reaction with DBCO-maleimide (Click Chemistry Tools).

Force Spectroscopy with Coincident Illumination. Our group has previously demonstrated high-stability and high-spatiotemporal-resolution methods for probing membrane-protein unfolding free energies by AFM (31, 33, 34). As in these prior studies, we used a commercial AFM (Cypher ES, Asylum Research) modified to have a detection laser spot size of 3 μm (37) and ultrashort AFM cantilevers (L = 9 μm) modified with a focused ion beam to have ~15 to 30 pN/nm spring constant, ~1 to 2 μs response time, a quality factor (Q) of ~0.5, and ~1 pN force stability over a 10-s averaging window as measured by Allen deviation (55). Cantilever stiffness was measured in air prior to chemical functionalization. An example of cantilever geometry and mechanical properties is shown in *SI Appendix*, Fig. S12. These cantilevers were chemically functionalized with azido-PEG_5-triethoxysilane (BroadPharm) (56). As in the prior work, we deposited purple membrane on freshly cleaved mica after dilution in absorption buffer [10 mM Tris HCl (pH 7.8), 300 mM KCl] and sonication for 3 min with an alternating protocol of 2 s on, 2 s off (Vibra-cell VCX, Sonics and Materials). To facilitate photoactivation, the mica was mounted atop a glass coverslip, which was in turn mounted to a metal sample disc with a hole bored in the center, and then to another sample disc with a cavity to accommodate an ultrathin 540-nm green LED (DURIS S5, OSRAM AG) (apparatus sketched in Fig. 2*A*). Wires leading to the LED were passed out of the closed AFM sample chamber using the magnetic pass-through terminals of the Cypher ES. We found that powering the LED directly from the AFM controller resulted in voltage drops in the AFM stage position sensors, so we instead used a 5-V gate signal from the AFM controller to trigger brief light pulses via the circuit shown in *SI Appendix*, Fig. S13. The key component was a precision-timing integrated circuit (NE555P, Texas Instruments). The intensity, duration, and period of the light pulses were set by varying potentiometers in the circuit.

After incubating the bR sample on the mica for 1 h, we rinsed with imaging buffer [10 mM Tris HCl (pH 7.8), 150 mM KCl] or, for the pH-9.5 measurements, an alternate buffer: 10 mM CHES (pH 9.5), 150 mM KCl. We used AFM imaging to locate membrane patches. On a given patch, we specified a grid of points spaced 5 to 10 nm apart and, at each point, attempted to probe bR by bringing the tip of the AFM cantilever into gentle contact with the surface (150 pN contact force, 3 s) and then retracting it. Observation of 150 pN force exerted on the cantilever during retraction indicated probable bR binding and triggered the data-acquisition protocol described in the main text and illustrated in *SI Appendix*, Fig. S2. Overall, a total of 2,940 dwells were examined with a total of 267 photoactivations across all assay conditions.

Classifying Photoexcited Behaviors. Individual 200-ms segments showing a light-induced perturbation in three-state unfolding/refolding equilibrium at a constant Z value were assigned as exhibiting destabilization or misfolding behavior based on energy-landscape criteria; although, only ~60% of all such events could be rigorously assigned by this method. We identified destabilizing behavior by one of two metrics. In the first, we looked for increased occupancy of states at higher L_0 with respect to those at lower L_0 (i.e., stabilization of I_G^2 with respect to I_G^1 and of I_G^1 with respect to I_G^0). In the second metric, used if all three states were not visible in the trace, we looked for *i*) energy-landscape minima of states I_G^0 and I_G^1 separated by a visible barrier and *ii*) the location of I_G^1 not shifted significantly to a different L_0 value. Likewise, misfolding was unambiguously determined by one of two metrics. In the first one, a state (I_G^{MF}) was stabilized with respect to all others. In the second, akin to the second destabilization metric above, we looked for a significant shift of I_G^{MF} away from I_G^1 in free-energy landscapes where a barrier was visible between I_G^0 and I_G^1 in the unexcited phase. Only those destabilizing and misfolded events that were unambiguously assigned by these metrics were used to generate the values in Table 1, the histogram of Fig. 4*B*, and the lifetime curves of Fig. 5*B*.

Energetic Analysis. Energy landscapes like those in Figs. 3*B* and 4*C* were generated from raw 5-MHz data by the following steps. First, data were down-sampled to 200 kHz resolution by smoothing with a 25-point second-order Savitzky–Golay filter (57) and retaining only every 12th point. Second, the force-extension curve of the full unfolding of bR (*SI Appendix*, Fig. S2, region 6) was fit by a wormlike chain (WLC) elastic model incorporating the PEG linker elasticity (58, 59); we used 0.4 nm as the persistence length of the unfolded amino-acid chain (60). Each point in force-extension space lies along a WLC curve having the parameters of this fit and a particular L_0. We thus converted our raw data into an L_0-vs-time trace. We observed some variation in overall L_0 values between molecules, which we attribute to variation in PEG linker length. Third, for a given 200-ms dwell at a particular Z, we constructed histograms of L_0 in both the closed and photoexcited phases. Finally, these probability distributions in L_0 [$P(L_0)$] were used to calculate energy landscapes using $-k_BT\ln[P(L_0)]$. Subsequent deconvolution was not essential to determine energetics between states because each minimum had approximately the same degree of curvature.

Determination of $\Delta\Delta G_{open}$ for the majority of records that did not exhibit three-state equilibrium in both the open and closed phases required separate analyses of the $I_G^0 \leftrightarrow I_G^1$ and $I_G^1 \leftrightarrow I_G^2$ transitions, which were then added (Table 1). To perform this analysis, we first fit the histograms of L_0 in each phase to multiple Gaussian functions as illustrated in *SI Appendix*, Fig. S3. Specifically, for a given constant-Z record, we fit the closed-phase histogram with the fewest number of Gaussian curves needed to reproduce the shape of the data using a common width, but allowed separate amplitudes (A) and centers for each Gaussian. We then fixed this same width when performing a similar fit of the open-phase histogram. The Gaussian amplitudes were used directly to calculate $\Delta\Delta G_{open}$ between states i and j according to:

$$\Delta\Delta G^{ij}_{open} = -k_BT \cdot \left\{ \ln\left(\frac{A_i}{A_j}\right) - \ln\left(\frac{A_i^*}{A_j^*}\right) \right\}, \qquad [3]$$

where asterisks denote values in the open phase. In cases where state I_G^1 was found to be best fit as a composite of two sub-states, the magnitudes of these were combined in this analysis.

Kinetic Analysis. Kinetic lifetime plots were generated using the complementary cumulative probability distribution of observing a phase duration longer than a specified time. Exponential fits were weighted by the number of surviving records represented by each point in the lifetime data.

For some misfolded data, the lifetime exceeded the 200-ms dwell length at a particular Z. For these cases, we took $t_{misfold}$ as the full duration until return to the closed phase, even though the force changed in subsequent dwells and additional light pulse(s) were applied. This could introduce some bias for lifetimes beyond 150 ms. But, we note that we still observed exponentially distributed lifetimes for the misfolded states (Fig. 5*B*). We also assumed that lifetimes do not depend on the force applied to helix G, which was not the same throughout our data-acquisition protocol (*SI Appendix*, Fig. S2). This assumption is reasonable to the extent that it is helices E and F, and not the tensioned helix G, that rotate during transitions into and out

of the open phase (7). The observation of single-exponential kinetics characterized by a single force-independent τ_{open} in Fig. 5*B* further justifies this assumption.

Structural renderings were made using VMD (61).

Data, Materials, and Software Availability. The data presented in this paper, including supplementary figures, are available via Dryad (62).

ACKNOWLEDGMENTS. We thank Jason Cleveland for suggesting the LED illumination geometry, Lyle Uyetake for preparing protein samples, James Bowie for providing the bR expression platform, and Carl Sauer for fabricating the LED assembly. This work was supported by the NSF [MCB-2139572, PHY-2317149], the National Institute of General Medical Science (NIH) [K99GM140439, to D.R.J.], and the National Institute of Standards and Technology (NIST). Mention of commercial products is for information only; it does not imply NIST's recommendation or endorsement. T.T.P. is a staff member of NIST's Quantum Physics Division. The content is solely the responsibility of the authors and does not necessarily represent the official views of the NIH.

Author affiliations: [a]JILA, National Institute of Standards and Technology and University of Colorado, Boulder, CO 80309; and [b]Department of Molecular, Cellular, and Developmental Biology, University of Colorado, Boulder, CO 80309

1. R. Santos *et al.*, A comprehensive map of molecular drug targets. *Nat. Rev. Drug Discov.* **16**, 19–34 (2017).
2. J. T. Marinko *et al.*, Folding and misfolding of human membrane proteins in health and disease: From single molecules to cellular proteostasis. *Chem. Rev.* **119**, 5537–5606 (2019).
3. J. K. Lanyi, Bacteriorhodopsin. *Annu. Rev. Physiol.* **66**, 665–688 (2004).
4. C. Wickstrand *et al.*, Bacteriorhodopsin: Structural insights revealed using X-ray lasers and synchrotron radiation. *Annu. Rev. Biochem.* **88**, 59–83 (2019).
5. E. Nango *et al.*, A three-dimensional movie of structural changes in bacteriorhodopsin. *Science* **354**, 1552–1557 (2016).
6. P. Nogly *et al.*, Retinal isomerization in bacteriorhodopsin captured by a femtosecond x-ray laser. *Science* **361**, eaat0094 (2018).
7. T. Weinert *et al.*, Proton uptake mechanism in bacteriorhodopsin captured by serial synchrotron crystallography. *Science* **365**, 61–65 (2019).
8. S. Subramaniam *et al.*, Protein conformational changes in the bacteriorhodopsin photocycle. *J. Mol. Biol.* **287**, 145–161 (1999).
9. A. P. Perrino, A. Miyagi, S. Scheuring, Single molecule kinetics of bacteriorhodopsin by HS-AFM. *Nat. Commun.* **12**, 7225 (2021).
10. E. Racker, W. Stoeckenius, Reconstitution of purple membrane vesicles catalyzing light-driven proton uptake and adenosine triphosphate formation. *J. Biol. Chem.* **249**, 662–663 (1974).
11. S. O. Smith *et al.*, Chromophore structure in bacteriorhodopsins–O640 photointermediate. *Biochemistry* **22**, 6141–6148 (1983).
12. R. H. Lozier, R. A. Bogomolni, W. Stoeckenius, Bacteriorhodopsin: A light-driven proton pump in Halobacterium Halobium. *Biophys. J.* **15**, 955–962 (1975).
13. B. Hessling, J. Herbst, R. Rammelsberg, K. Gerwert, Fourier transform infrared double-flash experiments resolve bacteriorhodopsin's M1 to M2 transition. *Biophys. J.* **73**, 2071–2080 (1997).
14. K. Ludmann, C. Gergely, G. Varo, Kinetic and thermodynamic study of the bacteriorhodopsin photocycle over a wide pH range. *Biophys. J.* **75**, 3110–3119 (1998).
15. M. J. Pettei, A. P. Yudd, K. Nakanishi, R. Henselman, W. Stoeckenius, Identification of retinal isomers isolated from bacteriorhodopsin. *Biochemistry* **16**, 1955–1959 (1977).
16. L. S. Brown, R. Needleman, J. K. Lanyi, Conformational change of the E-F interhelical loop in the M photointermediate of bacteriorhodopsin. *J. Mol. Biol.* **317**, 471–478 (2002).
17. N. A. Dencher, D. Dresselhaus, G. Zaccai, G. Buldt, Structural changes in bacteriorhodopsin during proton translocation revealed by neutron diffraction. *Proc. Natl. Acad. Sci. U.S.A.* **86**, 7876–7879 (1989).
18. S. Subramaniam, M. Gerstein, D. Oesterhelt, R. Henderson, Electron diffraction analysis of structural changes in the photocycle of bacteriorhodopsin. *EMBO J.* **12**, 1–8 (1993).
19. J. Vonck, Structure of the bacteriorhodopsin mutant F219L N intermediate revealed by electron crystallography. *EMBO J.* **19**, 2152–2160 (2000).
20. T. E. Thorgeirsson *et al.*, Transient channel-opening in bacteriorhodopsin: An EPR study. *J. Mol. Biol.* **273**, 951–957 (1997).
21. W. Xiao, L. S. Brown, R. Needleman, J. K. Lanyi, Y. K. Shin, Light-induced rotation of a transmembrane alpha-helix in bacteriorhodopsin. *J. Mol. Biol.* **304**, 715–721 (2000).
22. N. Radzwill, K. Gerwert, H. J. Steinhoff, Time-resolved detection of transient movement of helices F and G in doubly spin-labeled bacteriorhodopsin. *Biophys. J.* **80**, 2856–2866 (2001).
23. H. Kamikubo *et al.*, Structure of the N intermediate of bacteriorhodopsin revealed by x-ray diffraction. *Proc. Natl. Acad. Sci. U.S.A.* **93**, 1386–1390 (1996).
24. H. Luecke, B. Schobert, H. T. Richter, J. P. Cartailler, J. K. Lanyi, Structural changes in bacteriorhodopsin during ion transport at 2 angstrom resolution. *Science* **286**, 255–261 (1999).
25. H. J. Sass *et al.*, Structural alterations for proton translocation in the M state of wild-type bacteriorhodopsin. *Nature* **406**, 649–653 (2000).
26. J. Zhang *et al.*, Crystal structure of the O intermediate of the Leu93→Ala mutant of bacteriorhodopsin. *Proteins* **80**, 2384–2396 (2012).
27. G. Nass Kovacs *et al.*, Three-dimensional view of ultrafast dynamics in photoexcited bacteriorhodopsin. *Nat. Commun.* **10**, 3177 (2019).
28. M. Shibata, T. Uchihashi, H. Yamashita, H. Kandori, T. Ando, Structural changes in bacteriorhodopsin in response to alternate illumination observed by high speed atomic force microscopy. *Angew. Chem. Int. Ed. Engl.* **123**, 4502–4505 (2011).
29. M. Shibata, H. Yamashita, T. Uchihashi, H. Kandori, T. Ando, High-speed atomic force microscopy shows dynamic molecular processes in photoactivated bacteriorhodopsin. *Nat. Nanotechnol.* **5**, 208–212 (2010).
30. H. Yamashita *et al.*, Role of trimer-trimer interaction of bacteriorhodopsin studied by optical spectroscopy and high-speed atomic force microscopy. *J. Struct. Biol.* **184**, 2–11 (2013).
31. H. Yu, M. G. W. Siewny, D. T. Edwards, A. W. Sanders, T. T. Perkins, Hidden dynamics in the unfolding of individual bacteriorhodopsin proteins. *Science* **355**, 945–950 (2017).
32. P. R. Heenan, H. Yu, M. G. W. Siewny, T. T. Perkins, Improved free-energy landscape reconstruction of bacteriorhodopsin highlights local variations in unfolding energy. *J. Chem. Phys.* **148**, 123313 (2018).
33. H. Yu, D. R. Jacobson, H. Luo, T. T. Perkins, Quantifying the native energetics stabilizing bacteriorhodopsin by single-molecule force spectroscopy. *Phys. Rev. Lett.* **124**, 068102 (2020).
34. D. R. Jacobson, T. T. Perkins, Free-energy changes of bacteriorhodopsin point mutants measured by single-molecule force spectroscopy. *Proc. Natl. Acad. Sci. U.S.A.* **118**, e2020083118 (2021).
35. H. Yu, P. R. Heenan, D. T. Edwards, L. Uyetake, T. T. Perkins, Quantifying the initial unfolding of bacteriorhodopsin reveals retinal stabilization. *Angew. Chem. Int. Ed. Engl.* **58**, 1710–1713 (2019).
36. M. S. Bull, R. M. Sullan, H. Li, T. T. Perkins, Improved single molecule force spectroscopy using micromachined cantilevers. *ACS Nano* **8**, 4984–4995 (2014).
37. D. T. Edwards *et al.*, Optimizing 1-μs-resolution single-molecule force spectroscopy on a commercial atomic force microscope. *Nano Lett.* **15**, 7091–7098 (2015).
38. M. T. Woodside *et al.*, Direct measurement of the full, sequence-dependent folding landscape of a nucleic acid. *Science* **314**, 1001–1004 (2006).
39. J. Heberle, N. A. Dencher, Surface-bound optical probes monitor protein translocation and surface potential changes during the bacteriorhodopsin photocycle. *Proc. Natl. Acad. Sci. U.S.A.* **89**, 5996–6000 (1992).
40. S. Subramaniam, R. Henderson, Molecular mechanism of vectorial proton translocation by bacteriorhodopsin. *Nature* **406**, 653–657 (2000).
41. J. M. Baskin *et al.*, Copper-free click chemistry for dynamic in vivo imaging. *Proc. Natl. Acad. Sci. U.S.A.* **104**, 16793–16797 (2007).
42. G. I. Bell, Models for specific adhesion of cells to cells. *Science* **200**, 618–627 (1978).
43. S. Yohannan *et al.*, A C alpha-H···O hydrogen bond in a membrane protein is not stabilizing. *J. Am. Chem. Soc.* **126**, 2284–2285 (2004).
44. S. Yohannan *et al.*, Proline substitutions are not easily accommodated in a membrane protein. *J. Mol. Biol.* **341**, 1–6 (2004).
45. S. Faham *et al.*, Side-chain contributions to membrane protein structure and stability. *J. Mol. Biol.* **335**, 297–305 (2004).
46. N. H. Joh *et al.*, Modest stabilization by most hydrogen-bonded side-chain interactions in membrane proteins. *Nature* **453**, 1266–1270 (2008).
47. P. Curnow *et al.*, Stable folding core in the folding transition state of an alpha-helical integral membrane protein. *Proc. Natl. Acad. Sci. U.S.A.* **108**, 14133–14138 (2011).
48. J. P. Schlebach, N. B. Woodall, J. U. Bowie, C. Park, Bacteriorhodopsin folds through a poorly organized transition state. *J. Am. Chem. Soc.* **136**, 16574–16581 (2014).
49. H. Luecke, B. Schobert, H. T. Richter, J. P. Cartailler, J. K. Lanyi, Structure of bacteriorhodopsin at 1.55 Å resolution. *J. Mol. Biol.* **291**, 899–911 (1999).
50. H. Otto *et al.*, Aspartic acid-96 is the internal proton donor in the reprotonation of the Schiff base of bacteriorhodopsin. *Proc. Natl. Acad. Sci. U.S.A.* **86**, 9228–9232 (1989).
51. J. B. Ames, R. A. Mathies, The role of back-reactions and proton uptake during the N → O transition in bacteriorhodopsin's photocycle: A kinetic resonance Raman study. *Biochemistry* **29**, 7181–7190 (1990).
52. F. Oesterhelt *et al.*, Unfolding pathways of individual bacteriorhodopsins. *Science* **288**, 143–146 (2000).
53. D. R. Jacobson, L. Uyetake, T. T. Perkins, Membrane-protein unfolding intermediates detected with enhanced precision using a zigzag force ramp. *Biophys. J.* **118**, 667–675 (2020).
54. D. Oesterhelt, W. Stoeckenius, Isolation of the cell membrane of Halobacterium halobium and its fractionation into red and purple membrane. *Methods Enzymol.* **31**, 667–678 (1974).
55. J. K. Faulk, D. T. Edwards, M. S. Bull, T. T. Perkins, Improved force spectroscopy using focused-ion-beam-modified cantilevers. *Methods Enzymol.* **582**, 321–351 (2017).
56. R. Walder *et al.*, Rapid characterization of a mechanically labile α-helical protein enabled by efficient site-specific bioconjugation. *J. Am. Chem. Soc.* **139**, 9867–9875 (2017).
57. A. Savitzky, M. J. E. Golay, Smoothing and differentiation of data by simplified least squares procedures. *Anal. Chem.* **36**, 1627–1639 (1964).
58. R. Petrosyan, Improved approximations for some polymer extension models. *Rheol. Acta* **56**, 21–26 (2017).
59. F. Oesterhelt, M. Rief, H. E. Gaub, Single molecule force spectroscopy by AFM indicates helical structure of poly(ethylene-glycol) in water. *New J. Phys.* **1**, 6.1–6.11 (1999).
60. M. Rief, M. Gautel, F. Oesterhelt, J. M. Fernandez, H. E. Gaub, Reversible unfolding of individual titin immunoglobulin domains by AFM. *Science* **276**, 1109–1112 (1997).
61. W. Humphrey, A. Dalke, K. Schulten, VMD: Visual molecular dynamics. *J. Mol. Graph.* **14**, 27–38 (1996).
62. D. R. Jacobson, T. T. Perkins, Quantifying a light-induced energetic change in bacteriorhodopsin by force spectroscopy. Dryad. https://doi.org/10.5061/dryad.z08kprrm1. Deposited 10 January 2024.